AGU ADVANCING EARTH AND SPACE SCIENCES

JGR Solid Earth

Key Points:

- Mantle flow field associated with the spoon-shaped Banda slab is investigated using seismic azimuthal anisotropy measurements
- Observations can be explained by trench-parallel flow both in the mantle wedge and the sub-slab region
- Northeastward movement of the slab relative to the asthenosphere induces the two flow systems and leads to steepening of the southern slab

Layered Mantle Flow Field Associated With Plate Kinematics and Slab Modulation Underneath the Horseshoe-Shaped Banda Arc-Islands

Sijia Li[1], Fansheng Kong[1,2] ![ORCID], Kelly H. Liu[2] ![ORCID], and Stephen S. Gao[2] ![ORCID]

[1]Key Laboratory of Submarine Geosciences, Second Institute of Oceanography, Ministry of Natural Resources, Hangzhou, China, [2]Geology and Geophysics Program, Missouri University of Science and Technology, Rolla, MO, USA

Abstract The Banda arc-continent collision zone signifies one of the most seismically active and tectonically intricate zones. The high convergence rate across the region, coupled with the exceptionally arcuate arc and subducted slab, makes it an ideal locale for investigating interactions between plate (slab) kinematics and plastic flow in the asthenosphere, which can be diagnosed by seismic anisotropy from shear wave splitting analyses. In total, 206 pairs of splitting measurements using teleseismic SKS, SKKS, and PKS, along with 43 pairs using local S phases, are obtained by utilizing broadband seismic data from five permanent seismic stations. To reduce the ambiguity in determining the origin of anisotropy leading to the teleseismic splittings, which lack vertical resolution, crustal anisotropy is constrained according to the sinusoidal moveout of converted S phases at the Moho using receiver functions. A layered anisotropic structure based on joint analyses of the anisotropy measurements characterizing different depth layers suggests the presence of trench-parallel flow both in the mantle wedge and the sub-slab region. The northeastward motion of the slab, entrained by the fast-moving Australian Plate, deflects asthenospheric materials. The modulation results in trench-parallel plastic mantle flows and leads to the steepening of the southern portion of the asymmetric spoon-shaped Banda slab. In the shallower part of the sub-slab region, the northeastward Australian Plate motion produces simple shear in the transitional layer between the rigid lithosphere and the viscous asthenosphere. The shear deformation induces seismic anisotropy with resulting fast orientations in accordance with the plate motion direction.

Plain Language Summary The Banda region represents a nascent arc-continent collision with the Australian continental lithosphere. The volcanic arc and non-volcanic arc-islands display a unique horseshoe shape. The subducted slab is anomalously bent 180°, leading to a spoon-shaped morphology with a steeper southern portion. The role of the kinematics of the Australian Plate and this bent slab in shaping the asthenosphere is not clear. This study uses seismic anisotropy measured using data recorded over 14 years by five broadband seismic stations on the non-volcanic arc-islands to explore this intriguing problem. Results suggest that the northeastward movement of the Australian Plate makes asthenospheric materials flow along the depth contour of the slab, steepening the Banda slab's southern part. In the sub-slab region, the upper portion follows the movement direction of the Australian Plate, while the deeper part is influenced more by slab deflection, directing asthenospheric flow.

1. Introduction

The subduction along the nearly 6,000 km-long Sumatra-Java-Banda Trench (Figure 1) represents the southeastern portion of the Neo-Tethys tectonic domain (Ding et al., 2023). Starting in the end of Early Cretaceous around ~100 Ma, the northward convergence toward the Sunda Plate resulted in thousands of kilometers of oceanic lithosphere being subducted into the deep Earth. This front has reached a depth of ~1,500 km beneath Borneo (Ding et al., 2023; Hall & Spakman, 2015). Currently, the Australian Plate is moving north-northeast at a rate of ~70 mm/year (Figure 1) according to the plate motion model of NNR-MOREVEL56 (Argus et al., 2011), and is regarded as the fastest-moving continental tectonic plate in the world. In contrast to Sumatra and Java, deformations in Banda are dominated by arc-continent collision along the exceptionally arcuate Banda arc with nearly 180° curvature (Figure 1), and the formation mechanism is debated (Hinschberger et al., 2005; Spakman & Hall, 2010). A recent perspective involves a model associated with the subduction of the Banda embayment, whose eastern margin was arc-shaped and began to subduct around ~15 Ma (Spakman & Hall, 2010). The rapid
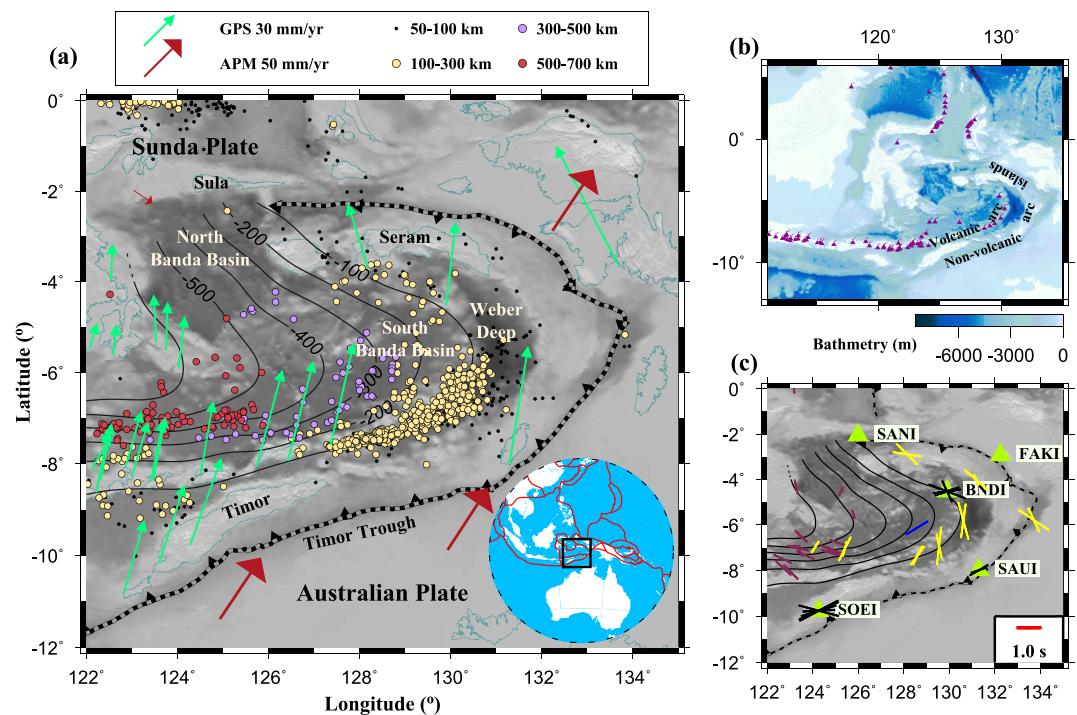
Figure 1. (a) Map showing the location of the study area with solid circles representing the epicenters of earthquakes with a magnitude greater than 5.0 occurred between 1980 and 2022. Green arrows indicate the Global Positioning System measurements, while red arrows denote the plate motion direction based on the NNR-MORVEL56 model (Argus et al., 2011). Black lines represent the depth contours of the Banda slab at intervals of 100 km (Hayes et al., 2018). The study area is enclosed in the inset map. (b) A bathymetric map of Southeast Asia highlighting both the volcanic arc and non-volcanic arc islands. Purple triangles mark active volcanoes. (c) Previous anisotropy measurements. The orientations of the bars correspond to the fast orientation and their lengths correlate with the size of the splitting time. The local S (dark red bars) and source-side splitting measurements (yellow bars) from Di Leo et al. (2012) are plotted at source locations, while the source-side splitting measurement from Wang and He (2020) depicted in blue bar is plotted at the surface bounce point of sS. Black bars signify the SKS and SKKS splitting measurements (C. W. Harris & Miller, 2022) plotted at station locations. Green triangles indicate the permanent seismic stations used in this study.

sinking, due to the negative buoyancy of the subducted lithosphere, resulted in the south-southeastward trench retreat to the dead-end of the embayment. This led to the opening of the North Banda and South Banda Basins in the back-arc region from 12.5 to 7.1 Ma and 6.5 to 3.5 Ma, respectively, and the formation of the arcuate Banda arc and a spoon-shaped slab (Spakman & Hall, 2010). One intriguing feature of the subducted slab is that the southern branch is significantly more vertical than the northern and eastern branches, forming an asymmetric spoon-shaped structure with the opening facing west (Figure 1).

After the subduction of the oceanic lithosphere, a portion of the continental Australian Plate has subducted beneath the Banda region, which has positive buoyancy and prevents further subduction (R. Harris, 2011; C. W. Harris & Miller, 2022). The northward movement of the Australian Plate and the resistance to subduction led to the arc-continent collision. This shift is evidenced by global positioning system observations that show a deceleration from 70 mm/year at the southern Timor Trough to 30 mm/year at Seram (Figure 1; Koulali et al., 2016). The collision between the arc-islands and the Australian continental margin causes the transition from an accretionary wedge to fold and thrust belts (R. Harris, 2011) and contributes to the formation of the spoon-shaped Banda slab and the 180° bend of the Banda arc (Spakman & Hall, 2010). Recent studies indicate the Banda slab is still folding, with asthenospheric materials bounded by the arcuate slab being pushed to the west (Wang & He, 2020; Wei et al., 2022). However, C. W. Harris and Miller (2022) identified a distinct mantle wedge flow field moving along the slab depth contour to the east beneath Timor and neighboring regions. Earlier research suggests that the mantle flow field in the sub-slab mantle along the arc-islands is parallel to the trench strike (Figure 1; Di Leo et al., 2012; C. W. Harris & Miller, 2022; Lynner & Long, 2014). This seems inconsistent with the widely held view that beneath a fast-moving tectonic plate, mantle flow is parallel to the plate motion

direction (Ba et al., 2023; Martin-Short et al., 2015). How plastic asthenospheric materials react to the pull of the rapidly moving Australian Plate and slab movements, potentially affecting slab morphology, is still unclear and requires more study. These scientific uncertainties might be partially resolved by imaging azimuthal seismic anisotropy, which can be reliably measured and characterized using shear wave splitting (SWS) analyses (Silver & Chan, 1991).

Seismic anisotropy is widely recognized as a common property in the upper mantle and is extensively used to examine and characterize deformations in both the lithosphere and asthenosphere (e.g., Ba et al., 2023; C. W. Harris & Miller, 2022; Kufner et al., 2018; Lin et al., 2016; Silver & Chan, 1991). Seismic anisotropy in the upper mantle is often attributed to the lattice preferred orientation (LPO) of olivine, which is a major component of the upper mantle under the pyrolite model (S. Zhang & Karato, 1995). Mantle flow in the asthenosphere, driven either by overriding plate motion (e.g., Ba et al., 2023) or large-scale pressure/density gradients (e.g., Lin et al., 2016), induces simple shear, generating the LPO of olivine and thereby seismic anisotropy. Under horizontal simple shear, the fast axis of olivine, corresponding to the highest wave speed, aligns with the flow direction under standard pressure and temperature conditions (S. Zhang & Karato, 1995), that is, *A*-, *C*-, and *E*-type LPO of olivine. *B*-type LPO, which results in the fast axis of olivine orthogonal to the flow direction, is expected to exist in a narrow zone adjacent to the tip of the mantle wedge above some subducting slabs where relatively low-temperature, water-rich, and high-stress are present (Jung & Karato, 2001). Anisotropy in the lithospheric mantle typically corresponds to fossil fabrics from past deformations or to the current compression stress field, with the fast axis oriented perpendicular to the primary compression direction (Silver, 1996). As it passes through an azimuthally anisotropic area, a nearly vertical S wave splits into two components, each with a unique propagation velocity and orthogonal polarization (Ando et al., 1983; Crampin & Booth, 1985). The shear wave that travels faster has a polarization direction (the fast orientation) in line with the fast axis. Due to velocity differences in an azimuthally anisotropic area, a time lag (splitting time) arises between the arrivals of the split fast and slow waves, correlating positively with the thickness and/or strength of the anisotropic medium.

Along the horseshoe-shaped Banda arc, seismic anisotropy in the mantle wedge and below the subducted slab has been examined using receiver-side S waves (Di Leo et al., 2012; C. W. Harris & Miller, 2022) and splitting analyses from source-side S waves (Di Leo et al., 2012; Lynner & Long, 2014; Wang & He, 2020; Figure 1). In the upper mantle above the subducted Banda slab, Wang and He (2020) suggest that asthenospheric materials are being pushed out due to the ongoing folding of the Banda slab. This conclusion is based on a singular measurement which perplexingly aligns with the arc strike (the blue bar in Figure 1c). Although source-side S splitting analyses generally align in their anisotropy measurements (Di Leo et al., 2012; Lynner & Long, 2014) and suggest trench-parallel mantle flow beneath the Banda slab, these measurements only capture anisotropy below the event focal depth. Therefore, layers above the focal depth remain elusive.

To thoroughly investigate deformations in the upper mantle of the Banda arc and to better understand related mantle dynamics, this study employed SWS of teleseismic SKS, SKKS, and PKS phases (collectively referred to as XKS) and local S waves methods widely accepted by earlier research (e.g., Di Leo et al., 2012; C. W. Harris & Miller, 2022; Kong et al., 2022; Silver & Chan, 1991). To pinpoint the origin of anisotropy responsible for XKS splittings, which lack vertical clarity, we measured entire crustal anisotropy using receiver functions based on the sinusoidal patterns of S phases converted from P phases at the Moho (Kong et al., 2016; Rumpker et al., 2014). As subsequent sections will show, combining anisotropy measurements from various depth layers can reduce interpretative ambiguities. This comprehensive examination of anisotropic structures beneath the Banda arc offers unique insights into the associated layered mantle flow field, illuminating the kinematics of the arc-continent collision and the formation of the distinctive Banda slab.

2. Data

The broadband seismic data utilized in this study were recorded by five permanent seismic stations (Figure 1) over the period of 2008–2022 and were requested from the GEOFON Data Center of the GFZ German Research Center for Geosciences. The criteria of requesting data used for the XKS splitting analysis (Liu & Gao, 2013) are as followed. (a) Events used for the SKS splitting analysis are within the epicentral distance range of 83°–180°, which are 95°–180° for SKKS, and 120°–180° for PKS (Figure 2a). (b) If the focal depth of events is less than 100 km, the cutoff magnitude was set as 5.6, which reduces to 5.5 for events with a greater focal depth.
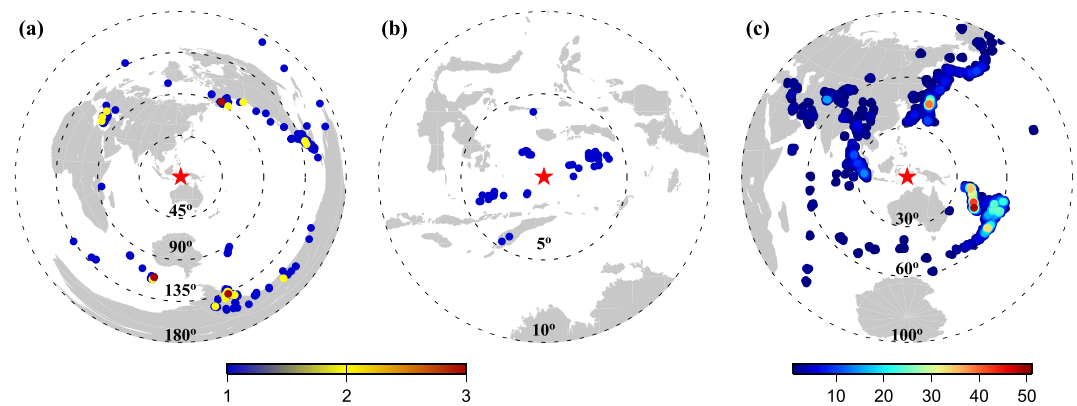
Figure 2. (a) Earthquake distribution for Quality A or B XKS splitting measurements. Each circle represents a circular bin characterized by a radius of 1° with the color denoting the number of measurements from earthquakes in the circle. (b) Same as (a) but for the local S splitting analysis. (c) Same as (a) but for the crustal anisotropy analysis using receiver functions. The color of the circles represents the number of receiver functions from earthquakes in the circle.

The epicentral distance range in the local S wave splitting analysis is 0°–7° and the cutoff magnitude is set as 4.0 (Figure 2b) (Kong et al., 2022). The splitting analysis using local S waves could be interfered by wave-type conversions from the free surface. To prevent the interference, only the local events which have an incidence angle smaller than θ are used, where θ is defined as $\sin^{-1} V_S/V_P$ (Evans, 1984) with the ratio between the P and S wave velocity set as 1.732 (Zandt & Ammon, 1995) and corresponds to a value of 35.3°.

In the process of requesting seismic data for the receiver function analysis to determine crustal anisotropy, the range of the epicentral distance is set as 30°–100° (Figure 2c), and the cutoff magnitude (M_C) is obtained by $M_C = M_{min} + (\Delta - \Delta_{min})/(180 - \Delta_{min}) - D/D_{max}$, where $M_{min} = 5.2$, and $\Delta_{min} = 30°$. Δ stands for the epicentral distance in degree, D_{max} represents the maximum focal depth of 700 km, and D denotes the focal depth of teleseismic events in kilometers (Kong et al., 2016). The distributions of events used in the receiver function and SWS analyses are shown in Figure 2.

3. Methods

3.1. Shear Wave Splitting Analyses

To measure the fast orientation (ϕ) and splitting time (δt) using the XKS phases, we employed the procedure developed by Liu and Gao (2013). The optimal pair of the fast orientation and splitting time is obtained by grid-searching candidate splitting parameters which have a range of 0°–180° and 0–3.0 s, and a step of 1.0° and 0.05 s, respectively, and corresponds to the values that can most effectively remove the energy within the time window on the corrected transverse component (Silver & Chan, 1991). The corner frequency parameters of band-pass filtering are initially set as 0.04 and 0.5 Hz to improve the signal-to-noise ratio (SNR), which is computed by $\max|A_{(a,f)}|/\max|A_{(a-10,f)}|$ (Liu et al., 2008), where $A_{(t1,t2)}$ stands for the maximum absolute value in the time window from t_1 to t_2 in units of seconds. a and f represent the beginning and end of the time window utilized to calculate the splitting parameters, which have initial values of $t_0 - 5$ s and $t_0 + 20$ s where t_0 denotes the predicted arrival time of the XKS phases based on the velocity model of IASP91. All the XKS splitting measurements are first automatically ranked to Quality A (excellent), B (good), C (unusable), N (null), and S (special) determined according to the SNRs on the radial and transverse components before and after corrections (Liu et al., 2008). Measurements ranked as N have outstanding XKS signal on the original radial component, but nearly no energy on the original transverse component (Figure S1 in Supporting Information S1). Those characterized by a rank of S have strong XKS signal on both the original radial and transverse components, but the XKS energy on the corrected transverse component cannot be effectively reduced during the analysis (Liu & Gao, 2013; Liu et al., 2008). Each of the measurements except those ranked as C is visually inspected and manually verified, during which process the rank, band-pass filtering parameters, and the beginning and end of the time window are adjusted if necessary. Totally, 1,310 measurements were manually examined, which include 409 SKS, 483 SKKS, and 418 PKS measurements. Examples of the XKS splitting measurement after the manual checking are shown in Figure 3.
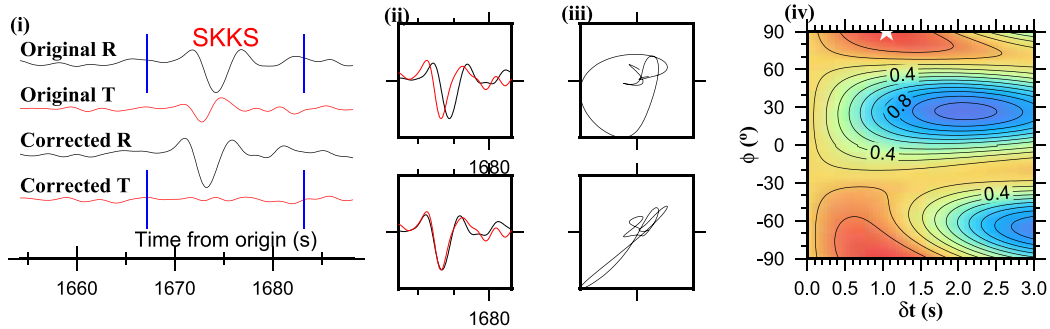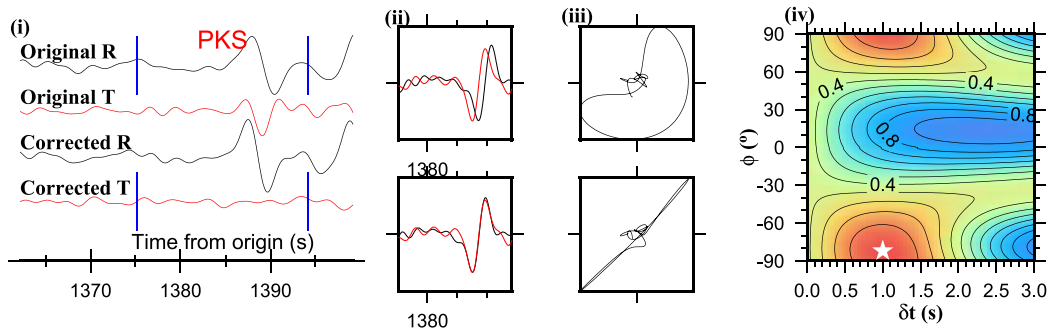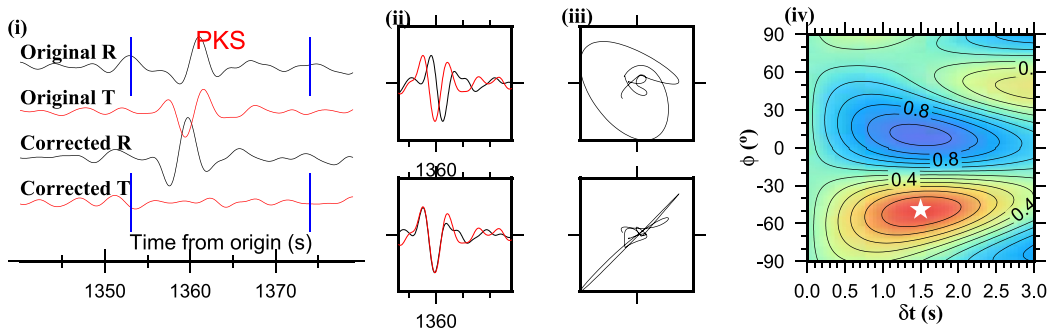
Figure 3. Shear wave splitting measurements obtained at Station FAKI. Note the significant differences in the splitting parameters from the three events. (i) Original radial component, original transverse component, radial and transverse components after corrections. (ii) Calculated fast (red) and slow (black) components using the optimal pair of splitting parameters before (top) and after correction (lower). (iii) Particle motion using the original radial and transverse components (top), and the motion based on the corrected components (lower). (iv) A misfit map which is obtained by calculating the energy on the corrected transverse component in the time window defined by the two vertical bars. The stars stand for the optimal pairs of splitting parameters corresponding to the minimum value on the map.

The technique used to measure the local S splitting parameters differs from that used for the XKS phases due to the unknown initial polarization for the former case. Accordingly, the optimal pair of local S splitting parameters is determined by computing two eigenvalues related to the covariance matrix (Silver & Chan, 1991), which corresponds to the minimum of the smaller eigenvalue and results in the most linear particle motion pattern. The band pass filtering parameters for the local S records are 0.1 and 1 Hz. To ensure that effective local S arrivals are included, the time window is initially set as $t_0 - 1$ s to $t_0 + 10$ s where t_0 here stands for the predicted local S arrival using the IASP91 velocity model. The local S splitting parameters went through the same automatic ranking procedure as the XKS phases. After the automatic ranking, the resulting 489 measurements underwent manual scrutiny and the time window and filtering parameters are adjusted if necessary in order to improve the SNR and exclude non-local S arrivals. Examples of local S splitting measurements are shown in Figure 4.
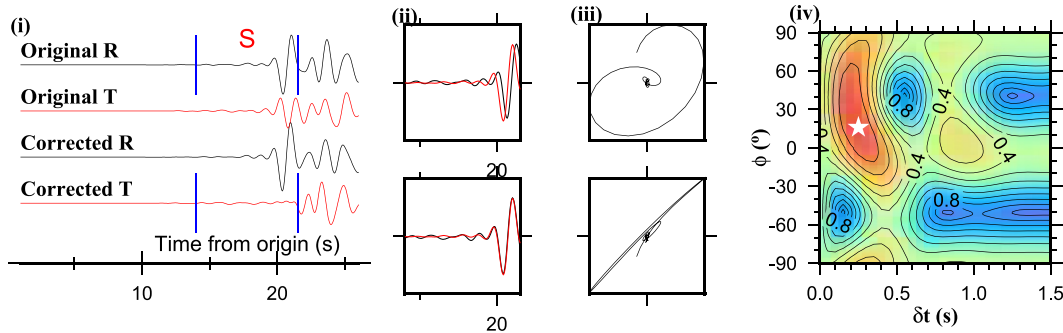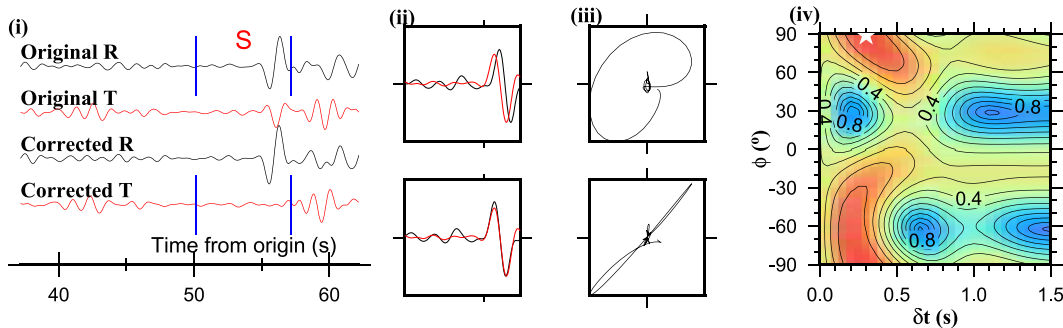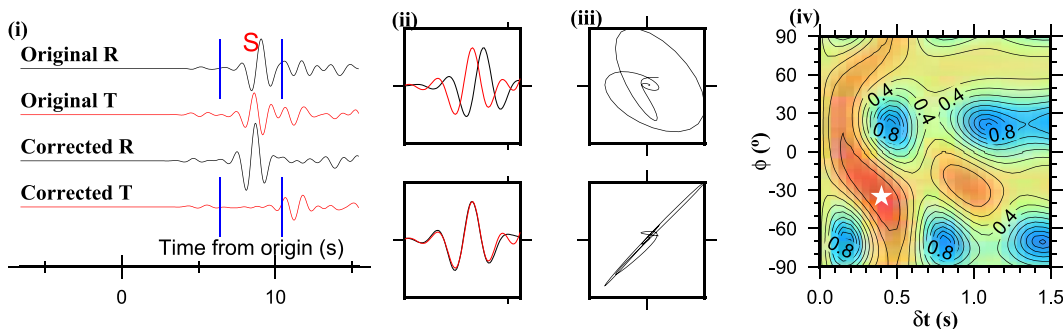
Figure 4. Same as Figure 3 but for local S splitting from Stations SOEI (a) and BNDI (b) and SANI (c). Note that the original radial and transverse components of the local S waves correspond to the predicted initial polarization direction that results in the optimal splitting parameters.

3.2. Crustal Anisotropy Parameters Inferred From Receiver Functions Analysis

The requested seismograms used for receiver function analysis were windowed 20 s before and 100 s after the first arrival of direct P wave, and were band-pass filtered using corner frequencies of 0.04 and 1.0 Hz (Kong et al., 2016). Only the seismograms with a SNR that is no less than 4.0 were used to obtain receiver functions based on the methodology in Ammon (1991). The SNR here is calculated based on $\max\left|A_{(a-8,a+12)}\right|/\left|\overline{A}_{(a-20,a-10)}\right|$, where a denotes the predicted direct P wave arrival time based on the IASP91 in seconds, and the numerator and the denominator represent the maximum and averaged absolute values in the corresponding time windows. The quality of the resulting receiver functions was examined and sorted based on the criteria associated with the SNR (details can be found in Kong et al., 2016). To eliminate the moveout of Moho P-to-S phases caused by the epicentral distance, all the high-quality radial receiver functions were corrected according to a uniform value of 60° for the epicentral distance, which next were grouped into 10°-wide back azimuth band to enhance the SNR. Crustal anisotropy is measured based on the sinusoidal pattern of the moveout of the converted S phases at the Moho when plotted against the back azimuth, which are achieved by applying a
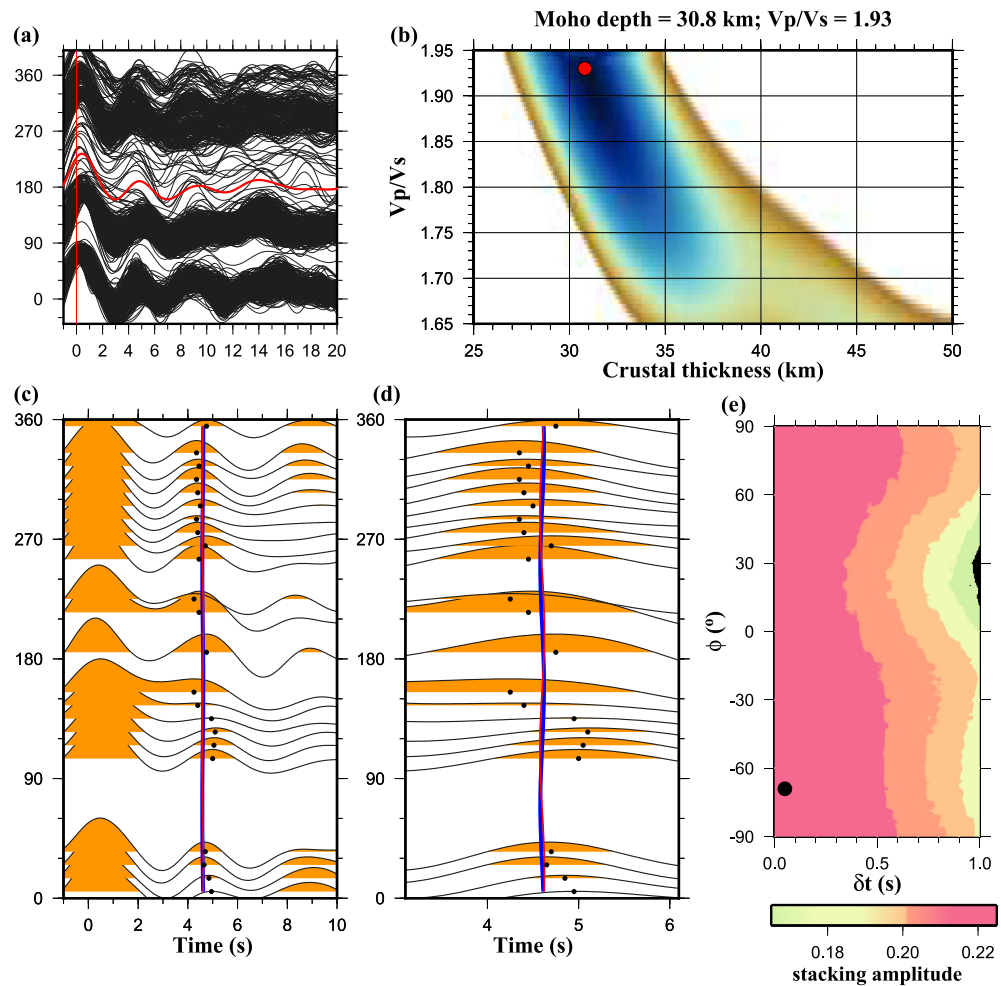
Figure 5. An example of crustal thickness and anisotropy measurement obtained at Station FAKI, showing weak crustal anisotropy. (a) Receiver functions (thin black traces) and a stacked trace (red trace). (b) Results from the *H-k* stacking analysis. (c) Azimuthal-band-averaged receiver functions with a width of 10°. The red and blue lines denote the predicted azimuthal variation of P-to-S conversions at the Moho using the optimal pairs of splitting parameters based on two independent procedures (Kong et al., 2016), with both of the resulting splitting times no greater than 0.05 s. (d) Same as (b) but with a time window ranging from 3.1 to 6.1 s. (e) A colored map showing the stacking amplitude of all candidate pairs of the splitting parameters with the optimal pair characterized by the largest value shown by the solid black dot.

procedure based on nonlinear fitting (Kong et al., 2016) and a stacking-based method (Rumpker et al., 2014). See Figure 5 for an illustration of crustal anisotropy measurement using seismic data from Station FAKI.

4. Results

4.1. XKS Splitting Measurements

Totally, this study obtained 206 pairs of the XKS splitting parameters at five long-running seismic stations (Figure 6 and Table S1). The numbers of measurements for SKS, SKKS, and PKS are 57, 67, and 82, respectively. The range of the resulting splitting time is 0.40–2.15 s with an average of 1.13 ± 0.34 s and the fast orientation has a range of 4.0°–139.0° and a circular mean of 92.5 ± 30.0°. The fast orientations generally accord with the strike of the Banda arc except Station SANI which exhibits mostly slab-contour-normal fast orientations (Figure 6). When plotted against the arriving azimuth of the teleseismic events, the splitting parameters from Stations FAKI and SOEI exhibit significant azimuthal variations, indicating the presence of complex anisotropy. As shown in Figure 7 and Figure S2 in Supporting Information S1, the azimuthal variations of the splitting parameters from Stations FAKI and SOEI are characterized by a periodicity of 90°, which are consistent with an anisotropy model
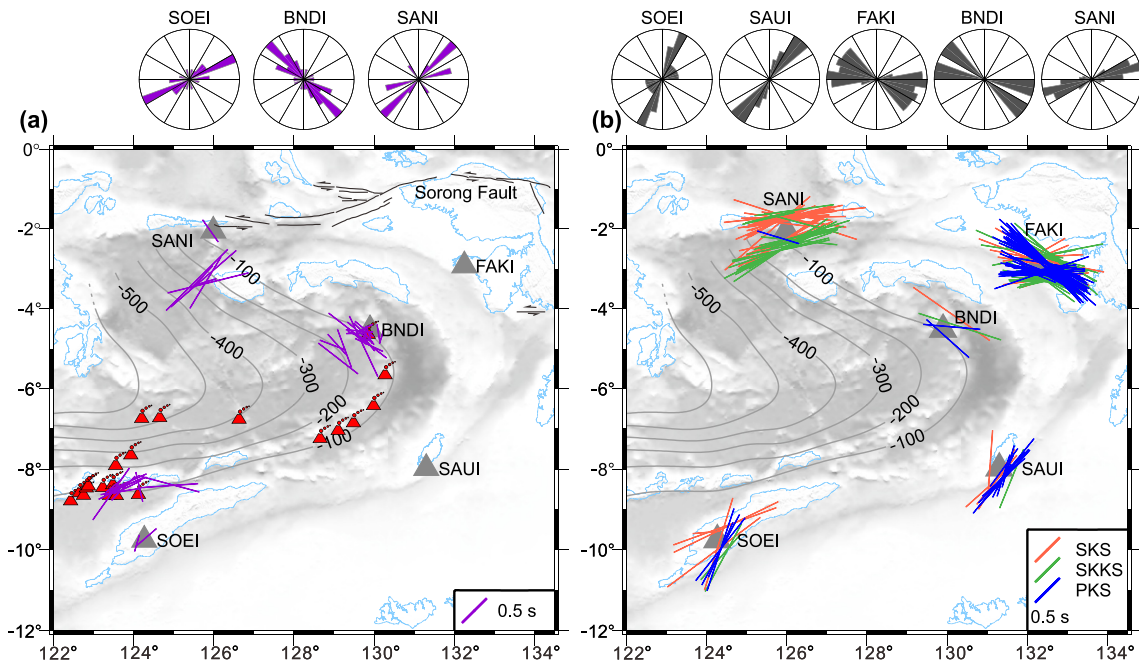
Figure 6. Resulting individual shear wave splitting parameters along the Banda Arc and adjacent areas using (a) local S and (b) teleseismic XKS phases. The bars are oriented along the fast orientation and scaled according to the splitting delay time. The local S splitting measurements are plotted at the midpoint between the station and event, while the XKS measurements are plotted at the ray-piercing point location at a depth of 250 km. The triangles represent locations of the stations with splitting measurements, and red volcano symbols in (a) indicate active volcanoes.
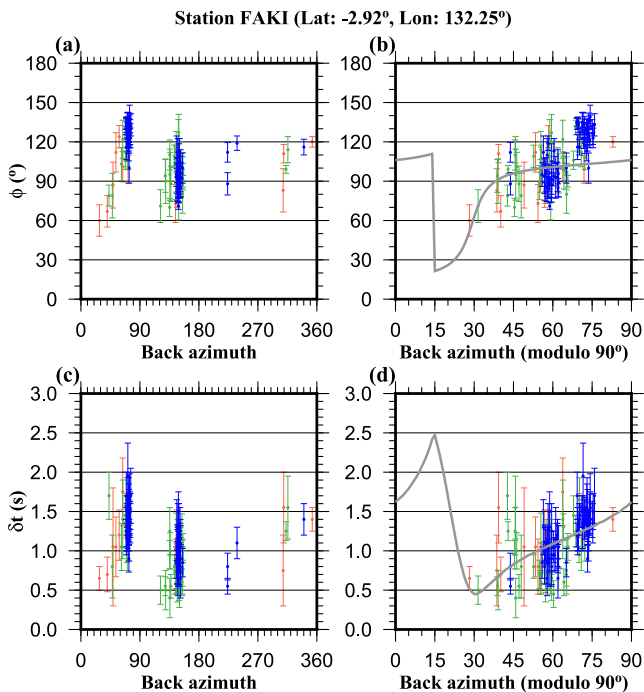

Figure 7. Fast orientation (a, b) and splitting time (c, d) measurements plotted with respect to the back azimuth (a, c) and modulo-90° back azimuth (b, d) for Station FAKI. Measurements from different phases are shown in distinct colors, same as Figure 6. The predicted azimuthal variations with respect to the back azimuth are shown in gray lines and calculated by using the optimal splitting parameters of the two layers and a uniform frequency of 0.2 Hz.

comprising two layers with non-orthogonal-and-non-parallel fast orientations (Silver & Savage, 1994). Examples of splitting measurements obtained at Stations FAKI and SOEI which are from different events but lead to significant difference of ϕ and δt are shown in Figure 3 and Figure S3 in Supporting Information S1, respectively. Here we would like to mention that the splitting measurements obtained using SKKS or PKS phases which were excluded by most of the previous SWS investigations in Banda (e.g., Di Leo et al., 2012; C. W. Harris & Miller, 2022) effectively enhance the azimuthal coverage and are crucial in identifying the presence of simple or complex anisotropy. By contrast, splitting parameters at Stations SAUI (Figure 8) and SANI (Figure S4 in Supporting Information S1) are generally azimuthally invariant, with the means of the parameters (Table 1) as (32.7 ± 12.2°; 0.90 ± 0.26 s) and (75.1 ± 13.7°; 1.25 ± 0.33 s), respectively, suggesting a single-layered anisotropy model.

Although Station BNDI has four pairs of well-defined SWS measurements (Figure S5 in Supporting Information S1), the measurements cover a wide back azimuth range and are azimuthally invariant, indicating a simple anisotropy model of single layer. In addition, null measurement observed at Station BNDI (Figure S1 in Supporting Information S1) also favors the presence of simple anisotropy, which is discerned at Stations SAUI and SANI as well.

4.2. Splitting Parameters in Two-Layered Anisotropy Model

In the case of an anisotropy model composed of two layers, the resulting SWS parameters appear to be indirect and, thus, cannot be used straightforwardly to probe anisotropic structures (Silver & Savage, 1994). The two-layered anisotropy parameters can be achieved by grid-searching all candidate fast
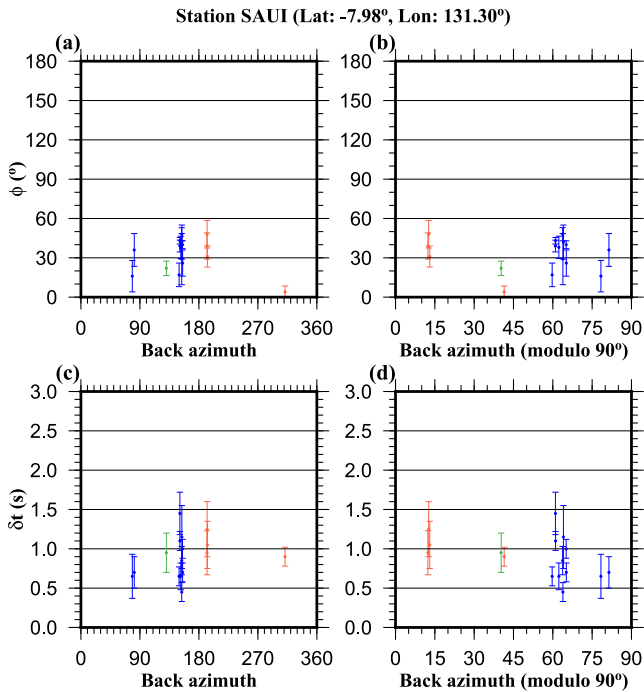
Figure 8. XKS splitting measurements from Station SAUI plotted against the back azimuth (a, c) and the modulo 90° back azimuth (b, d). Blue and green bars denote the PKS and SKKS splitting measurements, respectively, while bars in red show the SKS measurements.

orientations and splitting time values (Erman et al., 2022; Kong et al., 2018). The individual splitting parameters obtained at Stations FAKI and SOEI show a gradual variation across a broad back-azimuth range, and there is a notable difference in the fast orientations within a narrow back-azimuth band (Figure 7 and Figure S2 in Supporting Information S1). This suggests that applying the Bayesian grid-searching approach proposed in Kong et al. (2018) is feasible, as it can provide a priori constraints to diminish ambiguities in deducing the parameters of the two-layered anisotropy. The candidate values for the fast orientation of the lower layer ranged from $\phi_m - 30°$ to $\phi_m + 30°$ with a step of 1°, where ϕ_m stands for the circular mean of the fast orientations. The search range for the splitting time of the lower layer was set as $(\delta t_m - 0.3 \text{ s}, \delta t_m + 0.3 \text{ s})$ with an interval of 0.1 s and δt_m represents the average of the splitting times. For the upper layer, the splitting parameters were freely searched. For each candidate set of the four splitting parameters, a weighted misfit was obtained by computing the differences between the predicted individual splitting parameters and the observed values (Kong et al., 2018), that is,

$$\chi^2 = \sum_{i=1}^{N} \left\{ \omega_1 * \left[\Delta_a\left(\phi_i^{\text{obs}}, \phi_i^{\text{cal}}\right)/90.0 \right] + \omega_2 * \left[\left(\left| \delta t_i^{\text{obs}} - \delta t_i^{\text{cal}} \right| \right)/5.0 \right] \right\} * \omega_3(i) \tag{1}$$

where $\Delta_a\left(\phi_i^{\text{obs}}, \phi_i^{\text{cal}}\right)$ stands for the absolute value of the angular difference between the calculated and observed fast orientations, ω_1 (0.6) and ω_2 (0.4) are the weighting factors for the ϕ and δt, respectively, ω_3 (i) denotes the weighting factor used to correct for the uneven distribution of measurements in back azimuth, and N is the number of the SWS measurement pairs. The

misfit should reach the minimum at the optimal two pairs of the ϕ and δt, which are 117.0° and 1.55 s (lower layer), 45.0° and 0.60 s (upper layer) for Station FAKI, 71.0° and 1.65 s (lower layer), 23.0° and 0.60 s (upper layer) for Station SOEI (Table 1).

4.3. Results From Local S Splitting and Receiver Function Analysis

As depicted in Figure 6, 43 pairs of splitting parameters using local S phases were obtained at three stations (Table S2). The circular means of the fast orientations obtained at Stations SOEI, BNDI, and SANI are 59.5 ± 26.4°, 133.3 ± 27.7°, and 51.9 ± 29.8°, respectively, and the averages of the splitting time measurements are 0.56 ± 0.22 s, 0.42 ± 0.25 s, and 0.86 ± 0.44 s. As shown in Figure S6 in Supporting Information S1, the splitting times generally correlate with focal depth and raypath length until ∼300 km, suggesting that the source of anisotropy accounting for the local S splitting measurements mainly originates above 300 km. The relations between the splitting parameters and dominant frequency are weak (Figure S7 in Supporting Information S1), indicating insignificant frequency dependence. At Stations SOEI and BNDI, the fast orientations are generally consistent with the trench strike and slab depth contour. The splitting times generally correlate with the focal depth of the local events, indicating that the mantle wedge is anisotropic. At Station SANI, the fast orientations from deep events are nearly perpendicular to the depth contour of the Banda slab and the splitting times (with a mean of 0.93 ± 0.42 s) are slightly smaller than those from the XKS splitting analysis. The measurement from a shallow event originating near the Moho observed at SANI has a splitting time of 0.4 s and a fast orientation of 145 ± 1.5°. The fast orientation is roughly consistent with the strike of adjacent strike-slip fault (Figure 6) and could be attributed to shape preferred orientation of fluid-saturated fractures (Crampin, 1981) deformed by the fault (Figure 6).

Owing to the limited back azimuthal coverage of receiver functions at other stations, only Station FAKI yielded a reliable crustal anisotropy

Table 1
Resulting Teleseismic XKS Splitting Parameters

Station	Latitude (°)	Longitude (°)	ϕ (°)	δt (s)
BNDI	−4.52	129.90	115.1 ± 14.7	1.10 ± 0.30
SANI	−2.05	125.99	75.1 ± 13.7	1.25 ± 0.33
SAUI	−7.98	131.30	32.7 ± 12.2	0.90 ± 0.26
FAKI	−2.92	132.25	Upper: 45.0	Upper: 0.60
			Lower: 117.0	Lower: 1.55
SOEI	−9.76	124.27	Upper: 23.0	Upper: 0.60
			Lower: 71.0	Lower: 1.65

Note. The splitting parameters of Stations BNDI, SANI, and SAUI represent the averaged values of the individual parameters.
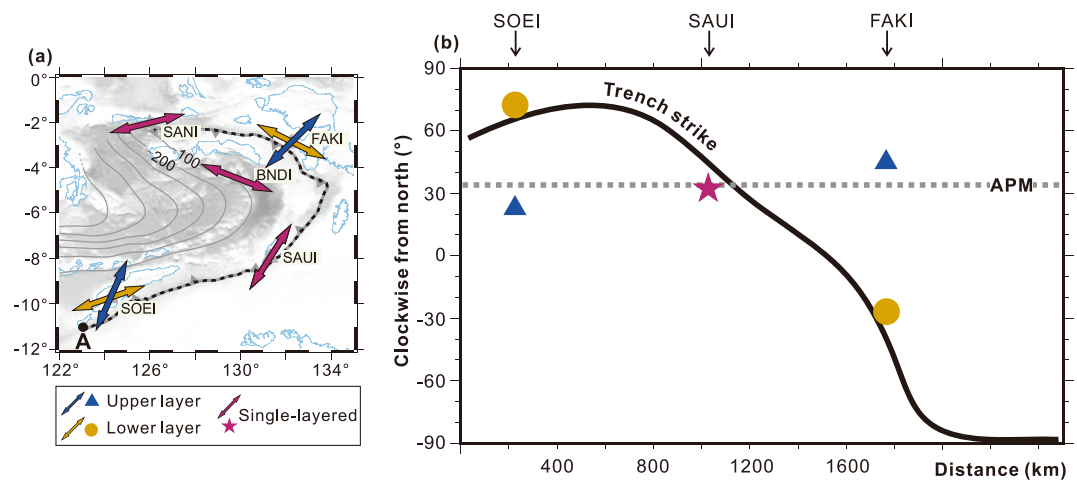
Figure 9. (a) Resulting fast orientations of two-layered anisotropy model at Stations SOEI and FAKI shown in double arrows plotted at station locations. The brown and blue double arrows respectively show the splitting parameters of the lower and upper layers, and the dark red arrows represent the station-averaged circular mean of the fast orientation at stations characterized by a single-layered anisotropy model. (b) Comparison of the Banda arc strike with the fast orientations plotted against the distance from Point A along the thrust fault boundary shown by the dashed line in (a). The triangles and dots respectively show the fast orientations of the upper layer and lower layers observed at Stations SOEI and FAKI, while the star shows the station-averaged fast orientation observed at Station SAUI. The APM direction is marked by the horizontal dashed line.

measurement. As depicted in Figure 5, the optimal values for the splitting time, derived from the application of two independent approaches, are both exceedingly minimal, not exceeding 0.05 s. This can be interpreted as a null measurement, signifying evidence of azimuthal isotropy throughout the crust beneath Station FAKI.

5. Discussions

5.1. Two-Layered Mantle Flow Underneath the Horseshoe-Shaped Banda Arc-Islands

The mantle flow field beneath the horseshoe-shaped Banda arc-islands is characterized by the local and XKS splitting measurements from stations near the trench, specifically Stations FAKI, SAUI, and SOEI. Past SWS research implies that beneath rapidly moving plates, mantle flow typically aligns with the plate motion direction (e.g., Ba et al., 2023; Kong et al., 2022; Martin-Short et al., 2015). This alignment suggests the existence of entrained flow, resulting in a fast orientation that matches the plate motion direction. Within subduction zones, this entrained mantle flow can be redirected due to the modulation of subducted slabs, leading to XKS fast orientations that align with trench strikes (e.g., Lynner & Long, 2013; Miller & Becker, 2012). To discern the impacts of these opposing forces, we first contrast the resulting fast orientations with both the trench strike and the APM direction. For easier comparison, we have illustrated the fast orientations on a profile that traces the trench from the south to the north. As depicted in Figure 9, the fast orientations of the lower layer align with the trench and arc strikes. In contrast, the upper layer's fast orientations generally match the absolute plate motion direction, as shown by the NNR-MOREVEL56 model (Argus et al., 2011). This coherence suggests a connection between the upper layer anisotropy and plate motion.

Given the parallelism between the lower layer fast orientations and the trench strike, and the consistency between the upper layer fast orientations and the APM direction (Figure 9), we propose an anisotropy model comprised of two layers. As illustrated in Figure 10, the anisotropy in the upper layer correlates with the movement of the rapidly advancing Australian Plate. This movement induces simple shear in the transitional layer between the lithosphere and the asthenosphere, resulting in the LPO of olivine. Deeper within the upper mantle, where the entraining force from plate motion diminishes with depth, asthenospheric materials become primarily influenced by the modulation of the subducted Banda slab. This leads to mantle flow that aligns with the trench strike (as seen in Figure 10). As shown below, the suggested anisotropy model aptly interprets the observed SWS measurements at Stations FAKI, SAUI, and SOEI.
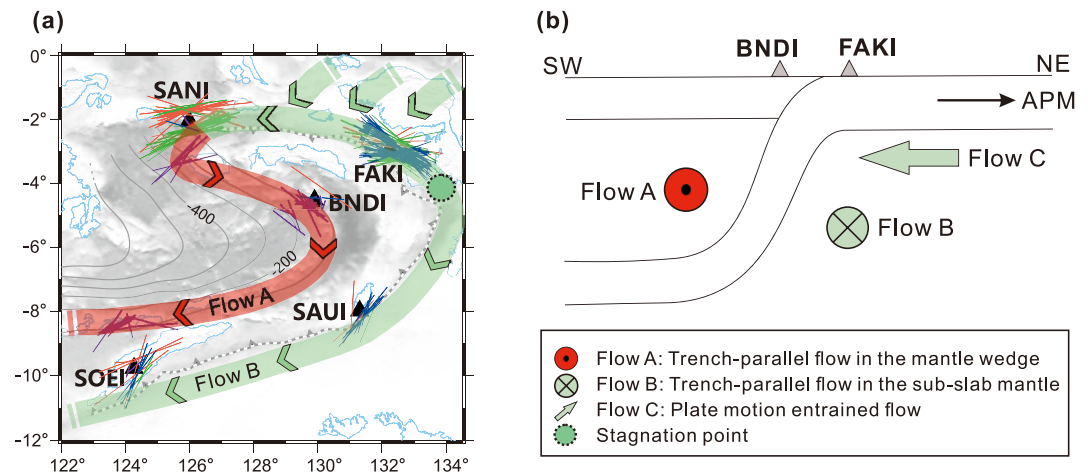
Figure 10. (a) A schematic map showing mantle flow field associated with the spoon-shaped Banda slab. Mantle flows in the mantle wedge (Flow A) and sub-slab region (Flow B) are both parallel to the trench strike, which are caused by the northeastward movement of the slab relative to the asthenosphere. Flow A enters the mantle wedge from the slab edge in the NW part of the subduction system, leading to trench normal fast orientations in the local S and teleseismic XKS splittings of Station SANI. The flow system moves along the slab contour and is responsible for trench-parallel fast orientations in local S splitting measurements at Stations BNDI and SOEI. Flow B is characterized by trench parallel XKS fast orientations and is related to the deflection and motion of the slab. (b) A schematic diagram showing a cross-section traversing Stations FAKI and BNDI. Flow C is responsible for APM-parallel upper layer anisotropy at SOEI and FAKI, which can be attributed to the entrainment of the fast-moving Australian Plate.

5.1.1. Station FAKI

Potential sources of anisotropy responsible for the XKS splittings at Station FAKI encompass the crust, lithospheric mantle, and the asthenosphere. Previous studies, such as the LITHO1.0 Model by Pasyanos et al. (2014), indicate that the lithosphere beneath Station FAKI extends to approximately 37 km (as seen in Figure S8 in Supporting Information S1). In this study, we apply the *H-k* stacking method (Zhu & Kanamori, 2000) to measure the crustal thickness at Station FAKI. Details regarding the data process and measuring procedures can be found in Gao et al. (2020). The crustal thickness from the *H-k* stacking analysis is 30.8 km (Figure 5), indicating that the mantle lithosphere is very thin. Moreover, the crustal anisotropy measurement from the receiver function analysis indicates an azimuthally isotropic crust which is characterized by a splitting time no larger than 0.05 s (Figure 5). The minimal crustal anisotropy, combined with the similarity in thickness between the crust and lithospheric mantle, implies that the anisotropy responsible for the XKS splittings is rooted beneath the rigid lithosphere. This observation aligns with the two-layered mantle flow model depicted in Figure 10. The anisotropy in the top layer, with a fast orientation of 45°, reflects the flow in the upper mantle layer due to simple shear associated with the plate motion with a rate of 70 mm/year, as seen in Figure 1. On the other hand, the anisotropy in the lower layer is a reflection of the mantle flow in that layer, responding to the northeastward shift of the slab relative to the asthenosphere, as illustrated in Figure 10.

5.1.2. Station SAUI

The XKS splitting measurements at Station SAUI are azimuthally invariant, an indication of the presence of a single-layered anisotropy model. The lithospheric thickness at Station SAUI is ~254 km based on the LITHO1.0 Model (Figure S8 in Supporting Information S1). Assuming the lithosphere is azimuthally anisotropic with a typical anisotropy strength of 4% (Savage, 1999), it is adequate to generate a splitting time that is comparable to the observed value (up to 1.45 s). Previous source-side splitting measurements (Di Leo et al., 2012) suggest that the sub-slab anisotropy is NNE-SSW oriented with splitting times in the range of 1.13–1.38 s, which are comparable to the observed values of the XKS splitting time. Therefore, an alternative cause for the XKS splittings involves the two-layered mantle flow model in Figure 10. Given the coherence between the direction of plate motion and the strike of the Banda arc at Station SAUI (Figure 9), the LPO corresponding to the two processes has the same orientation, leading to fast orientations that are characterized by an azimuthally invariant pattern (Figure 8) and consistent with the Australian Plate moving direction and the trench strike (Figure 9).

5.1.3. Station SOEI

At Station SOEI, the two local splitting measurements (49°, 0.4 s and 16°, 0.25 s) from events originating in the shallow slab are comparable to the anisotropy measurements from receiver function analysis (P. Zhang et al., 2022). The measurement of (49°, 0.4 s) which is orogen-parallel and has a larger splitting time, could be attributed to the LPO of anisotropic minerals in the lithosphere in response to the convergence (P. Zhang et al., 2022) or associated with fossil fabric formed during seafloor spreading. The other measurement which has a fast orientation in accordance with the convergence direction and a smaller splitting time can be caused by aligned fluid-saturated cracks (Crampin, 1981) deformed by NNE-SSW or NE-SW trending strike-slip faults (Duffy et al., 2013) in the upper crust.

The fast orientation of the upper layer anisotropy in the resulting optimal two-layered anisotropy model is generally consistent with the plate motion direction (Figure 9) and also with the fast orientation of the local S measurements from events originating in the shallow slab. The corresponding splitting times of the local S measurements range from 0.25 to 0.40 s with a mean of 0.33 s, which is smaller than that of the upper layer anisotropy of 0.60 s, indicating a portion of the upper layer anisotropy is from the sub-lithospheric mantle. Given the consistency between the upper layer fast orientation and the APM direction, and the parallelism between the lower layer and the trench strike, it is straightforward and feasible to attribute the two-layered anisotropy at Station SOEI to the layered mantle flow model illustrated in Figure 10.

5.2. Trench-Parallel Mantle Flow in the Mantle Wedge

The lithosphere beneath Station BNDI is less than 20 km according to the LITHO1.0 Model (Pasyanos et al., 2014). This suggests that any anisotropy in the lithosphere, if present, has a limited influence on the observed local S splitting measurements. Instead, the mantle wedge exhibits anisotropy with a fast orientation generally parallel to both the trench strike and the depth contour of the slab, as depicted in Figure 6. B-type LPO of olivine aligned by trench-normal flow (Jung & Karato, 2001) is not preferred as the dominant factor for the observed parallelism, simply because most of the local S and XKS ray paths do not traverse the forearc region of the mantle wedge where B-type LPO may develop (Figure 6a). Thus, the observed anisotropy can be safely explained by A-, C-, or E-type LPO aligned by trench-parallel flow. When combined with the local S splitting measurements from Station SOEI, we deduce that the plastic materials within the asthenospheric mantle wedge flow along the depth contour. This trench-parallel flow in the wedge mirrors the flow observed in the sub-slab mantle. It might arise from the northeastward motion of the slab relative to the asthenosphere, causing asthenospheric materials to enter the mantle wedge through the slab edge beneath Station SANI, where predominantly depth-contour-normal fast orientations are noticeable, as shown in Figure 10. Given that the local S splitting times are pervasively smaller than the XKS splitting measurements at Station BNDI, when combined with previous source-side splitting parameters (Figure 1c), we infer that the sub-slab mantle contains trench-parallel anisotropy as demonstrated by the mantle flow model illustrated in Figure 10. Slab anisotropy, if present, is similarly characterized by a fast orientation parallel to the slab depth contour.

The existence of horizontal mantle flow suggests that the vertical viscous flow, stemming from subduction of the slab, is currently weak, with the deeper portion of the slab resting in the deep mantle. The flat orientation of the slab diminishes both the vertical flow in the mantle above the slab and the resultant traction, thus currently reducing the associated dynamic topography and contributing to the uplift of the Banda basins (Husson et al., 2022). Another geodynamic implication of this inferred flow modulated by the slab could offer insights into deformations within the asthenosphere. Instead of being expelled due to folding of the slab from the arc-continent collision (Wang & He, 2020; Wei et al., 2022), asthenospheric materials, driven by the northeastward movement of the slab, are channeled into the mantle wedge. This results in flow patterns along the spoon-shaped contour of the slab, leading to fast orientations parallel to the depth contour of the slab. This deduced mantle flow suggests that folding of the arcuate Banda slab might have halted. The compression caused by the arc-continent collision might not currently extend to the asthenosphere and plays a limited role in folding the Banda slab. The flow within the mantle wedge could cause the southern branch of the Banda slab to become steeper, rendering it considerably more vertical than its northern and eastern counterparts, and thus producing an asymmetric spoon-shaped structure of the Banda slab, as depicted in Figure 1.

6. Conclusions

The complex anisotropic structures beneath the horseshoe-shaped Banda arc-islands are systematically explored using SWS and receiver function analyses. By jointly analyzing anisotropy measurements with three types of shear waves from different origin depths, we identify a layered anisotropic structure and mantle flow field beneath the horseshoe-shaped Banda arc-islands. The northeastward movement of the plate and slab, along with the modulation of the slab, cause materials in the asthenosphere to flow plastically along the Banda slab in both the mantle wedge and the sub-slab mantle, resulting in trench-parallel fast orientations of seismic anisotropy. The influx of asthenospheric materials into the mantle wedge may contribute to the steepening of the southern branch of the Banda slab. In the shallower portion of the sub-slab mantle, the seismic anisotropy has a fast orientation consistent with the plate motion direction, which can be adequately explained by entrainment of the Australian Plate.

Data Availability Statement

All the seismic waveform data used in this study were freely available from the GEOFON Data Center of the GFZ German Research Center for Geosciences (https://geofon.gfz-potsdam.de/waveform/archive; last accessed: January 2022) under network code GE (https://geofon.gfz-potsdam.de/waveform/archive/network.php?ncode=GE; Quinteros et al., 2021). Figures were made with Generic Mapping Tools version 4.5.18 (Wessel et al., 2019) and CorelDRAW 2021 (https://www.coreldraw.com/en/).

References

Ammon, C. J. (1991). The isolation of receiver effects from teleseismic P waveforms. *Bulletin of the Seismological Society of America*, *81*(6), 2504–2510. https://doi.org/10.1785/bssa0810062504

Ando, M., Ishikawa, Y., & Yamazaki, F. (1983). Shear wave polarization anisotropy in the upper mantle beneath Honshu, Japan. *Journal of Geophysical Research*, *88*(B7), 5850–5864. https://doi.org/10.1029/JB088iB07p05850

Argus, D. F., Gordon, R. G., & DeMets, C. (2011). Geologically current motion of 56 plates relative to the no-net-rotation reference frame. *Geochemistry, Geophysics, Geosystems*, *12*(11), Q11001. https://doi.org/10.1029/2011GC003751

Ba, K., Gao, S. S., Song, J., & Liu, K. H. (2023). Seismic azimuthal anisotropy beneath a fast moving ancient continent: Constraints from shear wave splitting analysis in Australia. *Journal of Geophysical Research: Solid Earth*, *128*(2), e2022JB025866. https://doi.org/10.1029/2022JB025866

Crampin, S. (1981). A review of wave motion in anisotropic and cracked elastic-media. *Wave Motion*, *3*(4), 343–391. https://doi.org/10.1016/0165-2125(81)90026-3

Crampin, S., & Booth, D. C. (1985). Shear-wave polarizations near the North Anatolian Fault - II. Interpretation in terms of crack-induced anisotropy. *Geophysical Journal of the Royal Astronomical Society*, *83*(1), 75–92. https://doi.org/10.1111/j.1365-246X.1985.tb05157.x

Di Leo, J. F., Wookey, J., Hammond, J. O. S., Kendall, J.-M., Kaneshima, S., Inoue, H., et al. (2012). Mantle flow in regions of complex tectonics: Insights from Indonesia. *Geochemistry, Geophysics, Geosystems*, *13*(12), Q12008. https://doi.org/10.1029/2012GC004417

Ding, W., Zhu, R., Wan, B., Zhao, L., Niu, X., Zhao, P., et al. (2023). Geodynamic processes of the southeastern Neo-Tethys Ocean and the formation mechanism of the curved subduction system in Southeast Asia. *Science China Earth Sciences*, *66*(4), 703–717. https://doi.org/10.1007/s11430-022-1071-4

Duffy, B., Quigley, M., Harris, R., & Ring, U. (2013). Arc-parallel extrusion of the Timor sector of the Banda Arc-continent collision. *Tectonics*, *32*(3), 641–660. https://doi.org/10.1002/tect.20048

Erman, C., Yolsal-Çevikbilen, S., Eken, T., Tilmann, F., Keleş, D., & Taymaz, T. (2022). Constraints on the lithospheric kinematics in the Aegean and western Anatolia unveiled by SKS splitting observations. *Journal of Geophysical Research: Solid Earth*, *127*(12), e2022JB025265. https://doi.org/10.1029/2022JB025265

Evans, R. (1984). Effects of the free surface on shear wavetrains. *Geophysical Journal International*, *76*(1), 165–172. https://doi.org/10.1111/j.1365-246X.1984.tb05032.x

Gao, J., Yu, Y., Song, W., Gao, S. S., & Liu, K. H. (2020). Crustal modifications beneath the central Sunda plate associated with the Indo-Australian subduction and the evolution of the South China Sea. *Physics of the Earth and Planetary Interiors*, *306*, 106539. https://doi.org/10.1016/j.pepi.2020.106539

Hall, R., & Spakman, W. (2015). Mantle structure and tectonic history of SE Asia. *Tectonophysics*, *658*, 14–45. https://doi.org/10.1016/j.tecto.2015.07.003

Harris, C. W., & Miller, M. S. (2022). Mantle flow deflected by arc–continent collision and continental subduction in eastern Indonesia. *Seismological Research Letters*, *93*(3), 1812–1834. https://doi.org/10.1785/0220210281

Harris, R. (2011). The nature of the Banda Arc–continent collision in the timor region. In *Arc-continent collision*. In *Frontiers in Earth sciences*. Springer. https://doi.org/10.1007/978-3-540-88558-0_7

Hayes, G. P., Moore, G. L., Portner, D. E., Hearne, M., Flamme, H., Furtney, M., & Smoczyk, G. M. (2018). Slab2, a comprehensive subduction zone geometry model. *Science*, *362*(6410), 58–61. https://doi.org/10.1126/science.aat4723

Hinschberger, F., Malod, J.-A., Rehault, J.-P., Villeneuve, M., Royer, J.-Y., & Burhanuddin, S. (2005). Late Cenozoic geodynamic evolution of eastern Indonesia. *Tectonophysics*, *404*(1–2), 91–118. https://doi.org/10.1016/j.tecto.2005.05.005

Husson, L., Riel, N., Aribowo, S., Authemayou, C., de Gelder, G., Kaus, B. J. P., et al. (2022). Slow geodynamics and fast morphotectonics in the far East Tethys. *Geochemistry, Geophysics, Geosystems*, *23*(1), e2021GC010167. https://doi.org/10.1029/2021GC010167

Jung, H., & Karato, S.-I. (2001). Water-induced fabric transitions in olivine. *Science*, *293*(5534), 1460–1463. https://doi.org/10.1126/science.1062235

Kong, F., Gao, S. S., Liu, K. H., & Li, J. (2022). Potassic volcanism induced by mantle upwelling through a slab window: Evidence from shear wave splitting analyses in Central Java. *Journal of Geophysical Research: Solid Earth*, *127*(3), e2021JB023719. https://doi.org/10.1029/2021JB023719

Kong, F., Wu, J., Liu, K. H., & Gao, S. S. (2016). Crustal anisotropy and ductile flow beneath the eastern Tibetan Plateau and adjacent areas. *Earth and Planetary Science Letters*, *442*, 72–79. https://doi.org/10.1016/j.epsl.2016.03.003

Kong, F., Wu, J., Liu, L., Liu, K. H., Song, J., Li, J., & Gao, S. S. (2018). Azimuthal anisotropy and mantle flow underneath the southeastern Tibetan Plateau and northern Indochina Peninsula revealed by shear wave splitting analyses. *Tectonophysics*, *747–748*, 68–78. https://doi.org/10.1016/j.tecto.2018.09.013

Koulali, A., Susilo, S., McClusky, S., Meilano, I., Cummins, P., Tregoning, P., et al. (2016). Crustal strain partitioning and the associated earthquake hazard in the eastern Sunda-Banda Arc. *Geophysical Research Letters*, *43*(5), 1943–1949. https://doi.org/10.1002/2016GL067941

Kufner, S.-K., Eken, T., Tilmann, F., Schurr, B., Yuan, X., Mechie, J., et al. (2018). Seismic anisotropy beneath the Pamir and the Hindu Kush: Evidence for contributions from crust, mantle lithosphere, and asthenosphere. *Journal of Geophysical Research: Solid Earth*, *123*(12), 10727–10748. https://doi.org/10.1029/2018JB015926

Lin, P. Y. P., Gaherty, J. B., Jin, G., Collins, J. A., Lizarralde, D., Evans, R. L., & Hirth, G. (2016). High-resolution seismic constraints on flow dynamics in the oceanic asthenosphere. *Nature*, *535*(7613), 538–541. https://doi.org/10.1038/nature18012

Liu, K. H., & Gao, S. S. (2013). Making reliable shear-wave splitting measurements. *Bulletin of the Seismological Society of America*, *103*(5), 2680–2693. https://doi.org/10.1785/0120120355

Liu, K. H., Gao, S. S., Gao, Y., & Wu, J. (2008). Shear wave splitting and mantle flow associated with the deflected Pacific slab beneath northeast Asia. *Journal of Geophysical Research*, *113*(B1), B01305. https://doi.org/10.1029/2007JB005178

Lynner, C., & Long, M. D. (2013). Sub-slab seismic anisotropy and mantle flow beneath the Caribbean and Scotia subduction zones: Effects of slab morphology and kinematics. *Earth and Planetary Science Letters*, *361*, 367–378. https://doi.org/10.1016/j.epsl.2012.11.007

Lynner, C., & Long, M. D. (2014). Sub-slab anisotropy beneath the Sumatra and circum-Pacific subduction zones from source-side shear wave splitting observations. *Geochemistry, Geophysics, Geosystems*, *15*(6), 2262–2281. https://doi.org/10.1002/2014GC005239

Martin-Short, R., Allen, R. M., Bastow, I. D., Totten, E., & Richards, M. A. (2015). Mantle flow geometry from ridge to trench beneath the Gorda–Juan de Fuca plate system. *Nature Geoscience*, *8*(12), 965–968. https://doi.org/10.1038/ngeo2569

Miller, M. S., & Becker, T. W. (2012). Mantle flow deflected by interactions between subducted slabs and cratonic keels. *Nature Geoscience*, *5*(10), 726–730. https://doi.org/10.1038/ngeo1553

Pasyanos, M. E., Masters, T. G., Laske, G., & Ma, Z. (2014). LITHO1.0: An updated crust and lithospheric model of the Earth. *Journal of Geophysical Research: Solid Earth*, *119*(3), 2153–2173. https://doi.org/10.1002/2013JB010626

Quinteros, J., Strollo, A., Evans, P. L., Hanka, W., Heinloo, A., Hemmleb, S., et al. (2021). The GEOFON Program in 2020 [Dataset]. *Seismological Research Letters*, *92*(3), 1610–1622. https://doi.org/10.1785/0220200415

Rumpker, G., Kaviani, A., & Latifi, K. (2014). Ps-splitting analysis for multilayered anisotropic media by azimuthal stacking and layer stripping. *Geophysical Journal International*, *199*(1), 146–163. https://doi.org/10.1093/gji/ggu154

Savage, M. K. (1999). Seismic anisotropy and mantle deformation: What have we learned from shear wave splitting? *Reviews of Geophysics*, *37*(1), 65–106. https://doi.org/10.1029/98RG02075

Silver, P. G. (1996). Seismic anisotropy beneath the continents: Probing the depths of geology. *Annual Review of Earth and Planetary Sciences*, *24*(1), 385–432. https://doi.org/10.1146/annurev.earth.24.1.385

Silver, P. G., & Chan, W. W. (1991). Shear wave splitting and subcontinental mantle deformation. *Journal of Geophysical Research*, *96*(B10), 16429–16454. https://doi.org/10.1029/91JB00899

Silver, P. G., & Savage, M. K. (1994). The interpretation of shear-wave splitting parameters in the presence of two anisotropic layers. *Geophysical Journal International*, *119*(3), 949–963. https://doi.org/10.1111/j.1365-246X.1994.tb04027.x

Spakman, W., & Hall, R. (2010). Surface deformation and slab–mantle interaction during Banda arc subduction rollback. *Nature Geoscience*, *3*(8), 562–566. https://doi.org/10.1038/ngeo917

Wang, L., & He, X. (2020). Seismic anisotropy in the Java-Banda and Philippine subduction zones and its implications for the mantle flow system beneath the Sunda plate. *Geochemistry, Geophysics, Geosystems*, *21*(4), e2019GC008658. https://doi.org/10.1029/2019GC008658

Wei, W., Zhao, D., Yu, W., & Shi, Y. (2022). Complex patterns of mantle flow in eastern SE Asian subduction zones inferred from P-wave anisotropic tomography. *Journal of Geophysical Research: Solid Earth*, *127*(5), e2021JB023366. https://doi.org/10.1029/2021JB023366

Wessel, P., Luis, J. F., Uieda, L., Scharroo, R., Wobbe, F., Smith, W. H. F., & Tian, D. (2019). The Generic Mapping Tools version 6 [Software]. *Geochemistry, Geophysics, Geosystems*, *20*(11), 5556–5564. https://doi.org/10.1029/2019GC008515

Zandt, G., & Ammon, C. J. (1995). Continental crust composition constrained by measurements of crustal Poisson's ratio. *Nature*, *374*(6518), 152–154. https://doi.org/10.1038/374152a0

Zhang, P., Miller, M. S., & Schulte-Pelkum, V. (2022). Tectonic fabric in the Banda Arc-Australian continent collisional zone imaged by teleseismic receiver functions. *Geochemistry, Geophysics, Geosystems*, *23*(6), e2021GC010262. https://doi.org/10.1029/2021GC010262

Zhang, S., & Karato, S. (1995). Lattice preferred orientation of olivine aggregates deformed in simple shear. *Nature*, *375*(6534), 774–777. https://doi.org/10.1038/375774a0

Zhu, L., & Kanamori, H. (2000). Moho depth variation in southern California from teleseismic receiver functions. *Journal of Geophysical Research*, *105*(B2), 2969–2980. https://doi.org/10.1029/1999JB900322